A robust method for generating inflow conditions for direct simulations of spatially-developing turbulent boundary layers

A. Ferrante, S.E. Elghobashi *

Department of Mechanical and Aerospace Engineering, University of California, Irvine, CA 92697, USA

Abstract

A method for generating inflow conditions for direct numerical simulations (DNS) of spatially-developing turbulent boundary layers is presented. The method is a modification of that of Lund et al. [J. Comput. Phys. 140 (1998) 233]. The approach of Lund et al. is based on having an auxiliary simulation (Code-A) in a three-dimensional domain similar to that of the main simulation (Code-B). The instantaneous velocity field on a selected plane in Code-A is used as the instantaneous inflow conditions for Code-B. The inflow conditions for Code-A are generated through a sequence of operations in which the velocity field at a downstream station is rescaled and re-introduced at the inlet plane. Our present method modifies the operations in Code-A by introducing a set of additional steps preceding the rescaling process. This set involves imposing at the inlet plane an appropriate spectrum $E(k)$ for the turbulence kinetic energy (TKE) and a condition for insuring that the statistical correlation $\langle u_1' u_3' \rangle$ between the streamwise and vertical velocity fluctuations retain a non-vanishing magnitude. This modification is essential for sustaining the production rate of TKE near the wall throughout the domain. Our DNS results obtained with the new modification are in excellent agreement with the experimental data of DeGraaff and Eaton [J. Fluid Mech. 422 (2000) 319] for $Re_\theta = 1430$.
© 2004 Elsevier Inc. All rights reserved.

1. Introduction

Direct numerical simulation (DNS) of a spatially-developing turbulent boundary layer (SDTBL) requires the solution of the three-dimensional, unsteady Navier–Stokes (NS) and continuity equations with their prescribed initial conditions and the conditions on the six boundaries of the computational domain. The most challenging boundary condition is that at the inlet plane. The reason is that in order to obtain accurate DNS results, the prescribed inflow values of the three time-dependent velocity components should *satisfy* the NS and continuity equations, i.e. they must be obtained a priori from *an auxiliary* DNS of the

---

* Corresponding author. Tel.: +1-949-824-6131; fax: +1-949-824-7326.
E-mail address: selghoba@uci.edu (S.E. Elghobashi).

same flow. This auxiliary simulation should be *synchronized* with the main simulation, such that at each time-step, the nodal (grid) values of the three velocity components on a plane at a fixed streamwise location in the auxiliary domain are copied to the corresponding nodes of the inlet plane of the main simulation. Lund, Wu and Squires [9], hereinafter referred to as LWS, reviewed the existing methods for generating the inflow conditions for SDTBL starting from the pioneering work of Spalart [13,14] and thus the reader is referred to that review. Spalart's method [13,14] eliminated the need for an auxiliary simulation by imposing *streamwise periodic boundary conditions* while accounting for the spatial growth of the SDTBL by adding source- or *growth*-terms to the NS equations. One advantage of the periodic boundary conditions is that they allow the Fourier discretization of the NS equations and hence improved accuracy. However, the additional *growth*-terms increased the complexity of the NS equations and required certain approximations to allow their evaluation.

LWS [9] proposed a modification to Spalart's method by eliminating the need for the growth-terms in NS equations and the periodicity in the streamwise direction, via a novel *rescaling* technique which accounts for the growth of the SDTBL. LWS's method requires an auxiliary simulation, hereinafter denoted as *Code-A*, in which the velocity field on a plane, referred to as *recycling plane*, near the domain exit is *rescaled* and introduced at the inlet plane as boundary condition (Fig. 1). The rescaling applies to the streamwise and vertical components of the mean velocity, and the three components of velocity fluctuation. The rescaling process is repeated until a satisfactory solution is obtained. Integration of the governing equations and rescaling proceed in time while storing, at each time step, the velocity components on a vertical plane in the middle of the domain of Code-A (Fig. 1) to be used later as inflow boundary conditions for the main simulation, hereinafter denoted as *Code-B*.

Although the LWS method [9] is a powerful technique that is much easier to implement than that of Spalart [13] we were not able to obtain a satisfactory development of the turbulent velocity correlations $\langle u_i' u_j' \rangle$ in Code-A when we used it in our DNS of SDTBL over a flat plate. However, it is clear from the paper of Lund et al. [9] that the LWS method works quite well in LES. Thus, the objective of the present paper is two fold:

(1) to introduce a different strategy for obtaining a satisfactory inlet turbulent velocity field for use with the LWS method; and
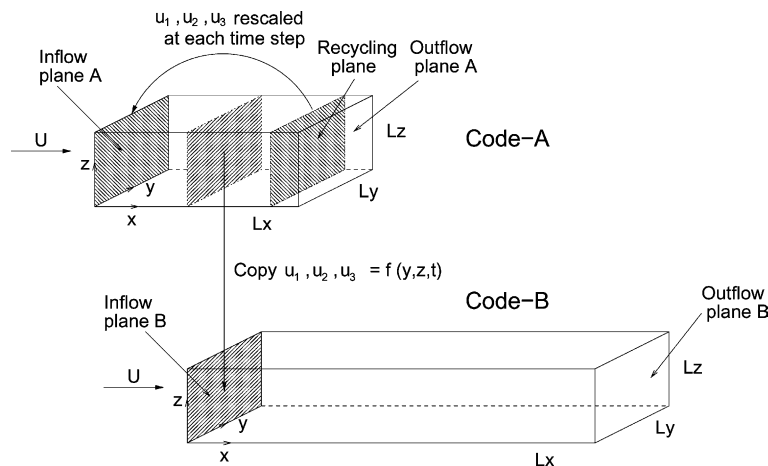

Fig. 1. A schematic of the computational domains of the auxiliary simulation (Code-A) and the main simulation (Code-B) used by Lund et al. [9] and in the present study for the generation of the inflow boundary conditions for SDTBL.

(2) to provide a detailed description of a procedure for generating the inflow conditions for Code-B which would be helpful to researchers using DNS of SDTBL.

The paper is organized as follows: Section 2 provides a mathematical description of our DNS of SDTBL including a detailed procedure for generating the inflow boundary conditions. Section 3 provides a comparison of our DNS results of SDTBL with the available experimental data. Closing remarks are presented in Section 4.

2. Direct simulation of a spatially-developing turbulent boundary layer

2.1. Governing equations

The governing equations for an incompressible turbulent boundary layer flow are the three-dimensional unsteady Navier–Stokes equations, which are given here in dimensionless form:

$$\frac{\mathrm{D}U_j}{\mathrm{D}t} = -\frac{\partial p}{\partial x_j} + v\frac{\partial^2 U_j}{\partial x_k\,\partial x_k}, \tag{1}$$

and the continuity equation,

$$\frac{\partial U_j}{\partial x_j} = 0, \tag{2}$$

where x_j are the streamwise x-, spanwise y- and wall-normal z-direction respectively for $j = 1, 2, 3$. The dimensionless kinematic viscosity is $v = 1/Re_\delta$ where $Re_\delta = \tilde{U}_\infty \tilde{\delta}_0/\tilde{v}$ is the Reynolds number based on the dimensional free-stream velocity $\tilde{U}_\infty$, the dimensional boundary layer thickness $\tilde{\delta}_0$ at the inlet plane ($x = 0$) of the main computational domain (Code-B in Fig. 1), and the dimensional kinematic viscosity $\tilde{v}$. All variables in (1) and (2) are non-dimensionalized by $\tilde{U}_\infty$ and $\tilde{\delta}_0$. It is advantageous for the numerical discretization of Eqs. (1) and (2) to split the *instantaneous* streamwise velocity component $U_1(x, y, z, t)$ into a prescribed reference velocity profile $U_{\mathrm{ref}}(z)$, which approximates the mean streamwise velocity $\langle U_1\rangle(x, z)$, and the deviation, u_1, of the instantaneous velocity in the x-direction from that reference velocity:

$$U_1(x, y, z, t) = U_{\mathrm{ref}}(z) + u_1(x, y, z, t). \tag{3}$$

Note that $\langle\cdots\rangle$ represents, throughout the paper, spatial averaging in the spanwise (y or x_2) direction in addition to time averaging of the enclosed quantity. Applying the velocity splitting (3) to (1) and (2), and denoting the instantaneous fluid velocities in the spanwise and wall-normal directions as u_2 and u_3 respectively, the momentum equations can be rewritten [3] as

$$\frac{\partial u_j}{\partial t} + \frac{\partial(u_j u_k)}{\partial x_k} + U_{\mathrm{ref}}\frac{\partial u_j}{\partial x_1} + u_3\delta_{j1}\frac{\mathrm{d}U_{\mathrm{ref}}}{\mathrm{d}x_3} = -\frac{\partial p}{\partial x_j} + v\left(\frac{\partial^2 u_j}{\partial x_k\,\partial x_k} + \delta_{j1}\frac{\mathrm{d}^2 U_{\mathrm{ref}}}{\mathrm{d}x_3^2}\right) \tag{4}$$

and the continuity equation:

$$\frac{\partial u_j}{\partial x_j} = 0, \tag{5}$$

where δ_{j1} is the Kronecker symbol.

Throughout the paper, dimensionless quantities in wall-units carry the superscript '+', i.e. $U_{\mathrm{ref}}^+ = U_{\mathrm{ref}}/u_\tau$ and $z^+ = zu_\tau/v$ where $u_\tau = \sqrt{\tau_{\mathrm{w}}/\rho}$ is the friction velocity, τ_{w} is the wall shear stress, and ρ is the fluid

density. The reference velocity in wall coordinates, U_{ref}^+, is prescribed according to the 'law of the wall' [1,10,15] as discussed in detail in the Appendix A.

2.2. Boundary conditions

The following conditions apply to both Code-A and Code-B (Fig. 1). Periodic boundary conditions were imposed in the spanwise *y*-direction for the velocity components and pressure. The no-slip boundary condition for the velocity components and Neumann condition for the pressure were imposed at the wall boundary,

$$u_1 = u_2 = u_3 = 0, \quad \frac{\partial p}{\partial z} = 0 \quad \text{at } z = 0. \tag{6}$$

The Neumann (stress-free) condition for the velocity components and Dirichlet condition for the pressure were imposed at the free-stream boundary,

$$u_1 = 0, \quad \frac{\partial u_2}{\partial z} = \frac{\partial u_3}{\partial z} = 0, \quad p = 0 \quad \text{at } z = L_z. \tag{7}$$

At the outflow plane ($x = L_x$) the following convective condition [8] was imposed for the velocity components,

$$\frac{\partial u_j}{\partial t} + U_c \frac{\partial u_j}{\partial x} = 0, \tag{8}$$

where U_c is the mean convective velocity at the exit plane. A zero-pressure gradient in the streamwise direction ($\partial p/\partial x = 0$) was imposed at both the inflow and outflow planes.

The prescription of the initial conditions throughout the domains and the turbulent flow conditions at the inlet plane of Code-A and Code-B are described in the following subsections.

2.3. Method for generating the inflow conditions for the auxiliary simulation: Code-A

Our method for generating the inflow conditions for Code-A comprises two main Tasks:

Task-1 requires the prescription of the spectrum, $E(k)$, of the turbulence kinetic energy (TKE) and the vertical, z or x_3, profiles of the four velocity correlations: $\langle u_1'^2 \rangle$, $\langle u_2'^2 \rangle$, $\langle u_3'^2 \rangle$, and $\langle u_1' u_3' \rangle$ at the inlet plane, $x = 0$. It should be emphasized here that u_i' is the deviation of the instantaneous velocity from $\langle U_i \rangle(x, z)$, i.e.

$$u_i'(x, y, z, t) = U_i(x, y, z, t) - \langle U_i \rangle(x, z). \tag{9}$$

The prescribed values of $E(k)$ and $\langle u_i' u_j' \rangle$ are then used in conjunction with the method of Le and Moin [6] to obtain the velocity field $u_i(x = 0, y, z)$ at time $t = 0$. The objective of Task-1 is to create a realistic distribution of the velocity field throughout the computational domain (Code-A) which is then used as an initial condition for Task-2.

Task-2 employs LWS's rescaling method to adjust the profiles of $\langle U_i \rangle$ and $\langle u_i' u_j' \rangle$ so that they match the growth rate of the SDTBL with the prescribed value of the momentum thickness Reynolds number, Re_θ, or the boundary layer thickness Reynolds number, Re_δ, at the inlet plane.

Task-1 is the *main* difference between our method and that of LWS [9]. More specifically, LWS recommended, instead of our Task-1, the prescription of only the mean velocity, $U_1(z)$, and a superposed random fluctuation, u_i', with a maximum amplitude of 10% of U_∞. Implementing that recommendation in our Code-A resulted in a fast temporal decay of $\langle u_i' u_j' \rangle$ throughout the domain and the consequent laminarization of the SDTBL. Our preliminary results indicated that the reason for that temporal decay was

that the rescaling of LWS was not able to sustain the required magnitude of the cross correlation $\langle u'_1 u'_3 \rangle$ necessary for the production of TKE when starting with the initial condition $\langle u'_1 u'_3 \rangle = 0$. We then attempted to rectify that problem by prescribing realistic profiles for the four correlations $\langle u'^2_1 \rangle$, $\langle u'^2_2 \rangle$, $\langle u'^2_3 \rangle$, and $\langle u'_1 u'_3 \rangle$ (see Appendix A in LWS [9]). However, the fast temporal decay of TKE persisted. Finally, we concluded that it was necessary to prescribe a realistic TKE spectrum $E(k)$ in addition to $\langle u'_i u'_j \rangle$ profiles at the inlet plane of Code-A in order to sustain the production rate of TKE. The combination of a realistic $E(k)$ and a non-vanishing $\langle u'_1 u'_3 \rangle$ in our method insures that the velocity-derivative skewness defined as

$$
S_u = \left[\frac{1}{3} \sum_{i=1}^{3} \langle (\partial u'_i / \partial x_i)^3 \rangle \right] \left[\frac{1}{3} \sum_{i=1}^{3} \langle (\partial u'_i / \partial x_i)^2 \rangle \right]^{-\frac{3}{2}} \tag{10}
$$

maintains a value of about -0.5 as shown in Fig. 2 where the instantaneous S_u was obtained by spatial averaging over the whole length and width of the domain and a height of $0 \leqslant z \leqslant 0.6\delta_0$. In contrast, the figure shows that the method of LWS produces a vanishing S_u as time increases. This skewness is related to the processes of vortex stretching and nonlinear energy transfer from small wavenumbers to large wavenumbers. Further evidence of the realism of the velocity field produced by our method is shown in Fig. 3(a) and (b) which displays the contours of the instantaneous correlation $u'_1 u'_3$ (white lines) superposed on the contours of the instantaneous vorticity component in the streamwise direction ω_x (color contour) on a vertical (yz) plane (near the exit) at $x = 8.25\delta_0$ and $t = 100$. Fig. 3(a) shows the zones of large magnitude of $u'_1 u'_3$ located between the counter-rotating longitudinal vortical structures. In contrast, Fig. 3(b) shows that the LWS method results in a vorticity of about three orders of magnitude less than that in our method, and the nearly vanishing $u'_1 u'_3$ is uniformly distributed in horizontal layers. Fig. 4 compares the realistic z^+ profiles of the velocity correlations $\langle u'_i u'_j \rangle$ at $x = 8.25\delta_0$ produced by our method in Code-A/Task-1 (lines) and those vanishingly small profiles of LWS (symbols).

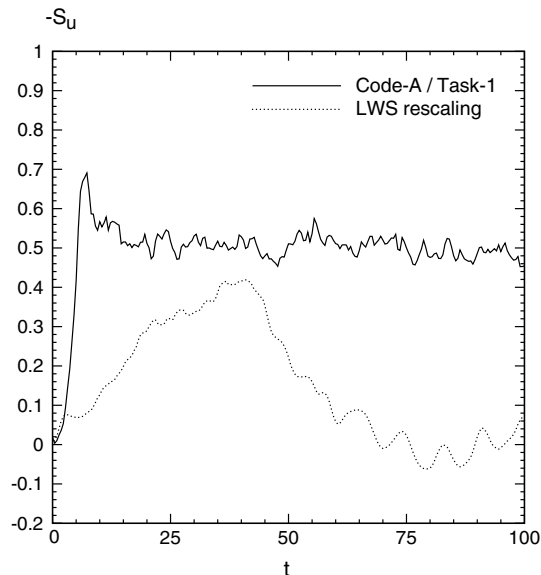We now describe in detail Tasks 1 and 2 of our method.

Fig. 2. Time development of the velocity-derivative skewness $-S_u$, Code-A/Task 1 (solid line); LWS rescaling (dotted line).
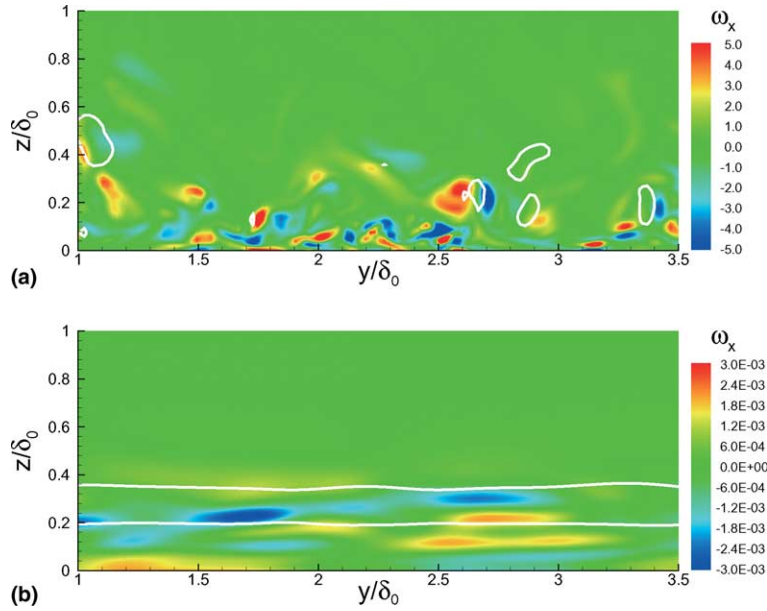
Fig. 3. Contours of the instantaneous correlation $u_1' u_3'$ (white lines) superposed on the contours of the instantaneous vorticity component in the streamwise direction ω_x (color contour) on a vertical (yz) plane at $x = 8.25\delta_0$ and $t = 100$. (a) Code-A/Task-1, $u_1' u_3' = -0.01$; (b) LWS rescaling, $u_1' u_3' = 2 \times 10^{-6}$.
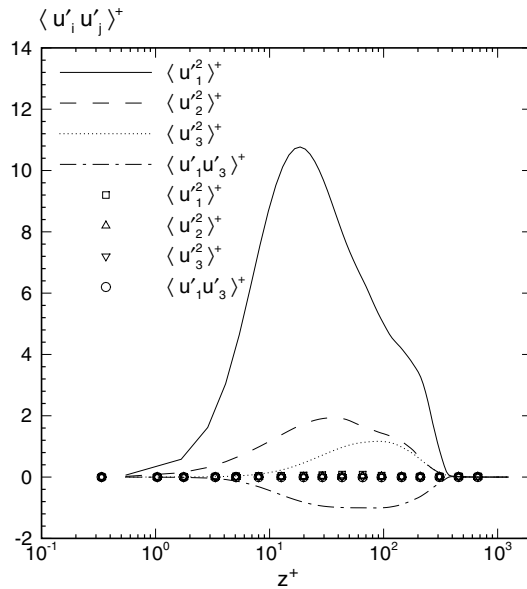

Fig. 4. z^+ profiles of the velocity correlations $\langle u_i' u_j' \rangle$ at $x = 8.25\delta_0$. Code-A/Task-1 (lines); LWS rescaling (symbols).

2.3.1. Task-1

We use the method of Le and Moin [6] for generating the inflow velocity fluctuations $u_1'(y, z, t)$, $u_2'(y, z, t)$ and $u_3'(y, z, t)$. The method of Le and Moin [6] is based on the approach of Lee et al. [7] but modified for

wall-bounded flows. Both methods require the prescription of the TKE spectrum, $E(k)$, at the inlet plane. Our $E(k)$ is different from that of Lee et al. [7].

The objective of Task-1 is to create initial conditions for Task-2 such that the LWS method produces the correct turbulent velocity field.

We list here the steps for implementing this method in detail for completeness.

(1) Prescribe a spectrum $E(k)$ of the TKE, e.g. for isotropic turbulence,

$$E(k) = \frac{k}{2\pi k_p^2} \exp\left(-\frac{k}{k_p}\right) \quad k = 1, \ldots, k_{max}, \tag{11}$$

where k is the wave number and k_p is the wave number of peak energy, and all the wave numbers are normalized by the lowest nonzero wave number, $\tilde{k}_{min}$. The streamwise wave number k_x is now converted into frequency ω, and thus the wave numbers k and $\tilde{k}_{min}$ can be written as

$$k = \frac{1}{\tilde{k}_{min}} \left[\left(\frac{2\pi\omega}{TU_\infty}\right)^2 + \left(\frac{2\pi k_y}{L_y}\right)^2 + \left(\frac{2\pi k_z}{L_z}\right)^2 \right]^{\frac{1}{2}} \tag{12}$$

and

$$\tilde{k}_{min} = \text{Min}\left\{ \frac{2\pi}{TU_\infty}, \frac{2\pi}{L_y}, \frac{2\pi}{L_z} \right\}, \tag{13}$$

where the time $T = \Delta t N_t$, and L_y and L_z are the spanwise and vertical lengths of the computational domain (Code-A) given in Table 1. The ranges for ω, k_y and k_z are $\omega = -N_t/2 + 1, \ldots, N_t/2$; $k_y = -N_y/2 + 1, \ldots, N_y/2$; and $k_z = -N_z/2 + 1, \ldots, N_z/2$, where N_t, N_y and N_z are given in Table 1. Thus the highest resolved wavenumber, k_{max}, is

$$k_{max} = \text{INT}\left\{ \frac{1}{\tilde{k}_{min}} \text{Min}\left\{ \frac{2\pi}{TU_\infty} \frac{N_t}{2}, \frac{2\pi}{L_y} \frac{N_y}{2}, \frac{2\pi}{L_z} \frac{N_z}{2} \right\} \right\}, \tag{14}$$

where $\text{INT}\{\cdots\}$ indicates the integer part of $\{\cdots\}$. The values of the parameters needed for Task-1 are listed in Table 1.

(2) Compute $\hat{E}(\boldsymbol{k})$, the kinetic energy at a given wavenumber vector, $\boldsymbol{k}$, from the prescribed spectrum $E(k)$ as follows.

The TKE spectrum $E(k)$ is defined as

$$E(k) = \sum_{k \leqslant |\boldsymbol{k}| < k+1} \hat{E}(\boldsymbol{k}), \tag{15}$$

where

$$\hat{E}(\boldsymbol{k}) = \langle \hat{u}_i^*(\boldsymbol{k}) \hat{u}_i(\boldsymbol{k}) \rangle / 2, \tag{16}$$

and $\hat{u}_i(\boldsymbol{k}, t)$ is the Fourier coefficient of $u_i'(y, z, t)$, and $\hat{u}_i^*(\boldsymbol{k}, t)$ is its complex conjugate. Thus $\hat{E}(\boldsymbol{k})$ can be computed from the prescribed $E(k)$ as

Table 1
Task-1 parameters

k_p	T	L_y	L_z	N_t	N_y	N_z	T_r	$\Delta\Phi_{max}$
4	$96\Delta t$	$5\delta_0$	$3.6\delta_0$	96	256	96	$24\Delta t$	$\pi/10$

$$\hat{E}(\boldsymbol{k}) = E(k)/Z(k), \tag{17}$$

where $Z(k)$ is the number of Fourier modes at wave number k,

$$Z(k) = \sum_{k \leqslant |\boldsymbol{k}| < k+1} 1. \tag{18}$$

(3) Compute the instantaneous $\hat{u}_i(\boldsymbol{k}, t)$ at every time step from

$$\hat{u}_i(\boldsymbol{k}, t) = [\hat{E}(\boldsymbol{k})]^{1/2} \exp[\mathrm{i}\Phi_i(\boldsymbol{k}, t)], \tag{19}$$

where Φ_i is a random phase angle and $\mathrm{i} = \sqrt{-1}$. Φ_i is a function of $\boldsymbol{k}$ and t, and is initialized at $t = 0$ as a random number for each $\boldsymbol{k}$. For $t > 0$, Φ_i is changed for each $\boldsymbol{k}$ only once in a given time interval T_r at a random instance by a random amount $\Delta\Phi_i$. Furthermore, $|\Delta\Phi_i|$ is bounded by a prescribed value $\Delta\Phi_{max}$. Table 1 provides the values of these parameters used in our simulation.

Fig. 5 compares the prescribed three-dimensional spectrum (11) and the spectrum generated from the Fourier coefficients via the sequence of Eqs. (19), (16) and (15). The displayed excellent agreement verifies the accuracy of our procedure for generating the Fourier coefficients for the non-cubic domain (see Eq. (12) and Table 1).

(4) Prescribe reasonable z-profiles for the four velocity correlations, $\langle u_1'^2 \rangle$, $\langle u_2'^2 \rangle$, $\langle u_3'^2 \rangle$ and $\langle u_1'u_3' \rangle$, e.g. from [13], which will be used below as reference profiles against which to check the velocity fluctuations u_i' computed via (19) to insure that they have the appropriate value of the correlation $\langle u_1'u_3' \rangle$.

(5) In order to insure that $\langle u_1'u_3' \rangle$ does not vanish, we need to rotate the flow coordinates $[x, z]$ by an angle θ_p so that they coincide with the principal coordinates $[\tilde{x}, \tilde{z}]$ where the corresponding velocities $\tilde{u}_1'$ and $\tilde{u}_3'$ are uncorrelated, i.e. $\langle \tilde{u}_1'\tilde{u}_3' \rangle = 0$. Compute the angle of rotation θ_p (see [6] for the derivation),

$$\theta_p(z) = \frac{1}{2} \tan^{-1} \left[\frac{2\langle u_1'u_3' \rangle}{\langle u_3'^2 \rangle - \langle u_1'^2 \rangle} \right]. \tag{20}$$
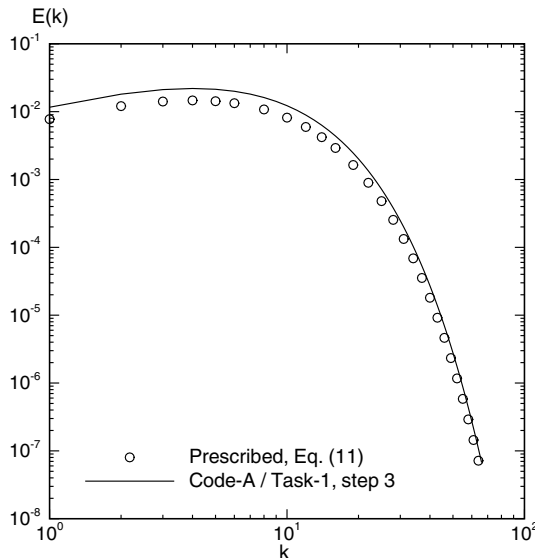

Fig. 5. Turbulence kinetic energy spectrum $E(k)$. Code-A/Task 1, step 3 (solid line); Prescribed, Eq. (11) (symbols).

Compute $\langle (\tilde{u}_1')^2 \rangle$ and $\langle (\tilde{u}_3')^2 \rangle$ in the principal coordinates as

$$\langle (\tilde{u}_1')^2 \rangle = \frac{\langle u_1'^2 \rangle \cos^2 \theta_p - \langle u_3'^2 \rangle \sin^2 \theta_p}{\cos^2 \theta_p - \sin^2 \theta_p},$$

$$\langle (\tilde{u}_3')^2 \rangle = \frac{\langle u_3'^2 \rangle \cos^2 \theta_p - \langle u_1'^2 \rangle \sin^2 \theta_p}{\cos^2 \theta_p - \sin^2 \theta_p}.$$

(21)

Note that since no rotation is required for u_2', the profile of $\langle (\tilde{u}_2')^2 \rangle$ is identical to the prescribed $\langle u_2'^2 \rangle$.

(6) Compute, at every time step, the inverse Fourier transform (complex to complex) of $\hat{u}_i(k_y, k_z, \omega)$ in the k_z direction to obtain $\hat{u}_i(k_y, z, \omega)$. Then evaluate the mean-square velocity correlation as

$$\overline{u_i'^2}(z) = \sum_{k_y = -N_y/2+1}^{N_y/2} \sum_{\omega = -N_t/2+1}^{N_t/2} \hat{u}_i(k_y, z, \omega) \hat{u}_i^*(k_y, z, \omega),$$

(22)

to compute the ratio $r_i(z)$ of the mean squares as

$$r_i(z) = \frac{\langle (\tilde{u}_i')^2 \rangle (z)}{\overline{u_i'^2}(z)}.$$

(23)

(7) Compute, at every time step, the inverse Fourier transform (complex to real) of $\hat{u}_i(k_y, z, \omega)$ in the k_y direction and sum the result over all frequencies ω to obtain $\tilde{u}_i'(y, z, t)$. Then multiply $\tilde{u}_i'(y, z, t)$ by $\sqrt{r_i(z)}$ so that the mean-square of the product matches $\langle (\tilde{u}_i')^2 \rangle (z)$ obtained from (21).

(8) Rotate $\tilde{u}_1'$ and $\tilde{u}_3'$ back to u_1' and u_3' in the flow coordinates $[x, z]$ using

$$u_1' = \tilde{u}_1' \cos \theta_p + \tilde{u}_3' \sin \theta_p,$$

$$u_3' = -\tilde{u}_1' \sin \theta_p + \tilde{u}_3' \cos \theta_p,$$

(24)

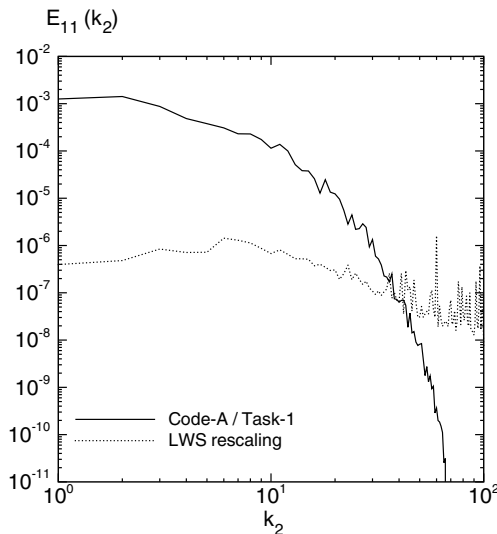to match the prescribed $\langle u_1' u_3' \rangle$ in step 4 above.

Fig. 6. One-dimensional energy spectrum $E_{11}(k_2)$ computed at $x = 0$ and $z^+ = 100$. Code-A/Task 1 (solid line); LWS rescaling (dotted line).

Steps 1, 2, 4 and 5 are performed only once, whereas steps 3, 6, 7, and 8 are performed at each time step to generate the inflow (boundary) conditions, $u_i'(y, z, t)$, of Code-A in Task-1.

The *initial* conditions for Task-1 were generated by copying the values of the inlet plane velocity fluctuations $u_i'(x = 0, y, z)$ at $t = 0$ to all other y–z planes of the computational domain (Code-A), plus a random fluctuation of maximum amplitude equal to 10% of $u_i'(x = 0, y, z)$. In order to insure that this *initial* velocity field satisfies the continuity equation (2) we solve the Poisson equation for the pressure:

$$\frac{\partial p}{\partial x_i \partial x_i} = \frac{1}{\Delta t} \frac{\partial u_j'}{\partial x_j}, \tag{25}$$

to obtain the velocity correction [12]: $\Delta u_j' = -\Delta t (\partial p / \partial x_j)$.

The numerical method for solving Eq. (25) as well as Eqs. (1) and (2) is described below in Section 2.5.2. The solution is advanced in time up to $t = 100 \simeq 1730 v / u_\tau^2$ when the flow field shows the characteristics of a SDTBL (see Figs. 2–4). The three-dimensional velocity field $u_i(x, y, z)$ at $t = 100$ is then stored for use as initial condition for Task-2.

It is important to show here the difference between the energy spectra generated in our Task-1 with that obtained from the method of Lund et al. [9] where the initial conditions were prescribed via only the mean velocity, $U_1(z)$, and a superposed random fluctuation, u_i', with a maximum amplitude of 10% of U_∞. Fig. 6 compares our time-averaged one-dimensional energy spectrum $E_{11}(k_2)$ in the y-direction at the inlet plane $(x = 0)$ at $z^+ = 100$ of Code-A/Task-1 with that obtained using LWS rescaling. It is clear that the latter, as expected, has a nearly uniform distribution of negligible energy over all wavenumbers, whereas our spectrum is realistic. Similar comparison was observed throughout the domain.

2.3.2. Task-2

Task-2 performs the following steps:

(1) Use the velocity field $u_i(x, y, z)$ stored in Task-1 at $t = 100$ as initial condition $(t = 0)$ for Task-2 simulation.

(2) Solve the NS and continuity equations (1) and (2) as described in Section 2.5.2 while using LWS's method of rescaling to generate the inlet conditions at each time step (see Lund et al. [9] for details). The *recycling* y–z plane (see Code-A domain in Fig. 1) used for rescaling the velocity field is fixed at $x_{rec} = 8.25 \delta_0$. At each time step the velocity field $u_i(x_{save}, y, z)$ on the y–z plane in the middle of the domain $(x_{save} = 5 \delta_0)$ is stored for use as instantaneous inlet condition for Code-B simulation.

The solution is advanced in time up to time $t = 300 \simeq 5200 v / u_\tau^2$, and the statistics are computed every 10 time steps during the time interval $150 \leqslant t \leqslant 300$. Fig. 7(a) and (b) shows the evolution in Code-A and Code-B of the boundary layer thickness δ, shape factor H, boundary layer displacement thickness δ^* and momentum thickness θ versus Re_θ from $Re_\theta = 800$ to 1500. It is important to note that there are no differences in the slopes of development of these four quantities in the overlap region $Re_\theta = 1020$ to 1200.

2.4. Inflow and initial conditions for the main simulation: Code-B

Code-B simulation is performed via the following steps:

(1) Copy $u_i(x_{save}, y, z)$ stored at $t = 0$ in Code-A/Task-2 into $u_i(x = 0, y, z)$ of Code-B (Fig. 1). Then, generate *initial* condition for Code-B by copying the values of the velocity of the inlet plane $u_i(x = 0, y, z)$ at $t = 0$ to all other y–z planes of the computational domain (Code-B), plus a random fluctuation of maximum amplitude equal to 10% of $u_i(x = 0, y, z)$.

(2) Correct the initial velocity field $u_i(x, y, z)$ by $\Delta u_j' = -\Delta t (\partial p / \partial x_j)$ as described above in Section 2.3.1 to insure that the continuity equation is satisfied throughout the domain.
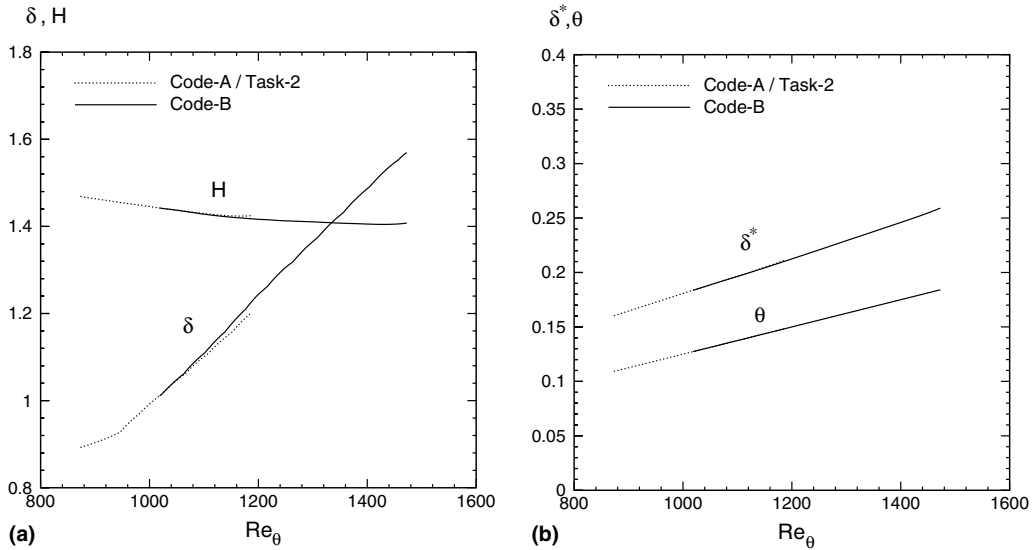
Fig. 7. (a) boundary layer thickness δ and shape factor H versus Re_θ; (b) boundary layer displacement thickness δ^* and momentum thickness θ versus Re_θ. Code-A/Task 2 (dotted lines); Code-B (solid lines).

(3) Solve the NS and continuity equations (1) and (2) as described in Section 2.5.2, while copying at each time step, as inlet conditions, the velocity field $u_i(x_{save}, y, z, t)$ stored in Code-A/Task-2.

Code-B simulation is *synchronized* with Code-A/Task-2, thus as in Code-A/Task-2 the solution in Code-B is advanced in time up to time $t = 300 \simeq 5200\nu/u_\tau^2$, and the statistics are computed every 10 time steps for $150 \leqslant t \leqslant 300$.

Results of Code-B are presented in Section 3.

2.5. Numerical method

The details of the numerical method are given in the next subsections.

2.5.1. Computational domain and grid

The computational domains, sketched in Fig. 1, are parallelepipeds whose dimensions L_x, L_y and L_z, and the corresponding numbers of grid points, N_x, N_y and N_z in the streamwise, spanwise and wall-normal directions respectively are listed in Table 2. The computational mesh is equispaced in the streamwise and spanwise directions, with grid spacing $\Delta x^+ = 14$ and $\Delta y^+ = 7$, whereas in the vertical direction, the mesh is stretched gradually to have a fine grid in the wall region, and a coarser grid outside the boundary layer

Table 2
Dimensions of the computational domain, L_x, L_y and L_z, and number of grid points, N_x, N_y and N_z in the streamwise, spanwise and wall-normal directions respectively

Code	L_x	L_y	L_z	N_x	N_y	N_z
A	$10\delta_0$	$5\delta_0$	$3.6\delta_0$	256	256	96
B	$20\delta_0$	$5\delta_0$	$3.6\delta_0$	512	256	96

($z > \delta$) where the mean flow is uniform. The stretched mesh has been created via mapping a uniform computational grid ζ into its non-uniform counterpart z with a combination of hyperbolic tangent functions [6]:

$$z = L_z \left[1 - \frac{\tanh \gamma (L_z - \zeta)}{\tanh \gamma L_z} \right] \quad 0 < z, \ \zeta < L_z, \tag{26}$$

where γ is a constant which determines the degree of grid compression near the wall boundary and L_z is the height of the computational domain. The closest grid point to the wall is located at $z_{min}^+ = 0.58$ and the maximum grid spacing is $\Delta z_{max}^+ = 34$ for the following values of the parameters: $\gamma = 0.66$, $L_z = 3.6\delta_0$ and $N_z = 96$. The spatial derivatives $\partial/\partial x_3$ in Eqs. (4) and (5) can be written via Eq. (26) as

$$\frac{\partial}{\partial z} = \left[\frac{\tanh \gamma L_z}{\gamma L_z} \cosh^2 \gamma (L_z - \zeta) \right] \frac{\partial}{\partial \zeta}. \tag{27}$$

2.5.2. Numerical discretization

The governing equations (Eqs. (4) and (5)) were discretized in space in an Eulerian framework on a staggered mesh [5] using a second-order central-difference scheme, except for the mean advection terms ($U_{ref} \partial u_j/\partial x_1$), which were evaluated via a fifth-order upwind differencing scheme. Time integration was performed via the second-order Adams–Bashforth scheme with a time step $\Delta t = 0.15\nu/u_\tau^2$. Pressure was treated implicitly and was obtained by solving the Poisson equation in finite-difference form [4] using a cosine transform in the streamwise direction [16], a fast Fourier transform (FFT) in the spanwise direction, and Gauss elimination in the wall-normal direction [11].

3. Results

Fig. 8 shows the spatial development in the streamwise direction in Code-B (Fig. 1) of the boundary layer thickness δ, the momentum thickness Reynolds number Re_θ, and the skin friction coefficient $C_f = 2\tau_w/\rho U_\infty^2$. It is seen that δ and Re_θ grow nearly linearly along x, whereas C_f decreases slightly due to the increase of Re_θ along the plate from 1020 to 1480.

We now compare our DNS results obtained from Code-B with the experimental data of DeGraaff and Eaton [2] for a SDTBL over a flat plate at $Re_\theta = 1430$. Figs. 9 and 10 display the comparison in wall units for the mean streamwise velocity and three Reynolds stresses. The DNS profiles shown in Fig. 9 were obtained by spatial averaging in the spanwise (y) direction at $x = 18.8\delta_0$ where $Re_\theta = 1430$ (Fig. 8), in addition to time-averaging over a nondimensional time $t = 150 \simeq 2600\nu/u_\tau^2$. The mean velocity profile is in excellent agreement with the experimental profile. Similar agreement is shown for the normal Reynolds stresses $\langle u_1'^2 \rangle$ and $\langle u_3'^2 \rangle$. The difference in the magnitude of the peak of turbulent shear stress, $\langle u_1'u_3' \rangle$, is probably due to experimental uncertainty. DeGraaff and Eaton [2] indicate a 10% error in the measured value of $\langle u_1'u_3' \rangle$. A similar discrepancy was found by [2] in comparing their results with the DNS results of [13] ($Re_\theta = 1410$). Our computed skin friction coefficient ($C_f = 3.96 \times 10^{-3}$) at $Re_\theta = 1430$ is nearly identical to that measured ($C_f = 3.97 \times 10^{-3}$) by DeGraaff and Eaton [2].

We have also performed a grid refinement test, by doubling the number of grid points in the streamwise direction (from $N_x = 512$ to $N_x = 1024$, keeping $L_x = 20\delta_0$) such that $\Delta x^+ = \Delta y^+ = 7$, and accordingly halved the time step (from $\Delta t = 0.150\nu/u_\tau^2$ to $\Delta t = 0.075\,\nu/u_\tau^2$) for the integration of Eqs. (4) and (5). Figs. 9 and 10 compare the results of the two grids used for Code-B and show that the finer mesh produces better agreement with the experimental data, and indicate that the maximum differences are: 1.8% for $\langle U_1 \rangle^+$, 4.7%
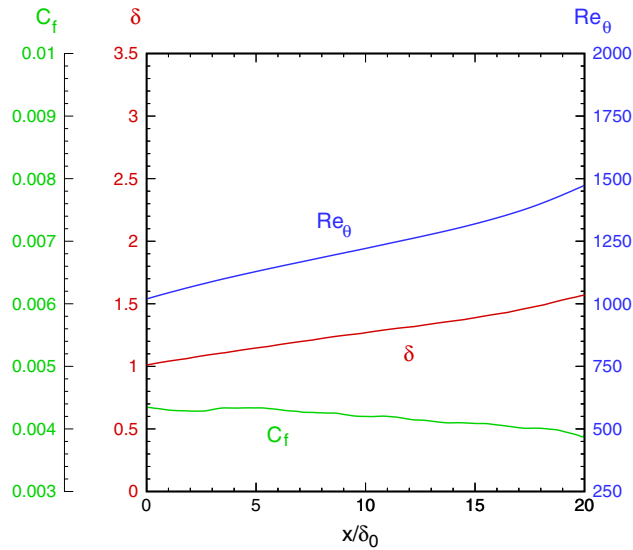
Fig. 8. Spatial development in the streamwise direction x of the boundary layer thickness δ, the skin friction coefficient C_f, and the Reynolds number based on the momentum thickness Re_θ. Code-B (solid lines).
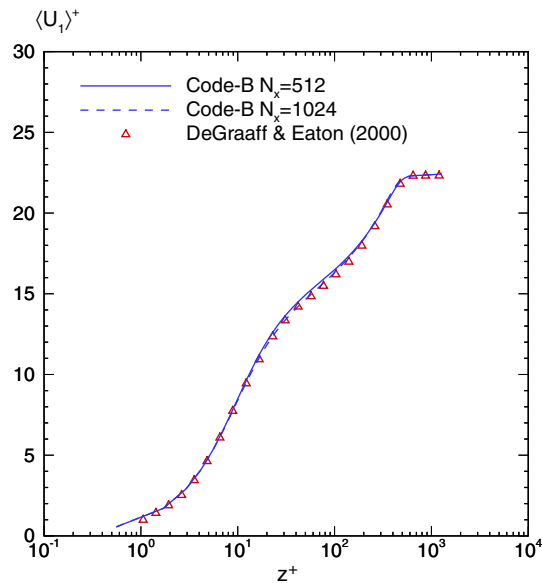

Fig. 9. Mean streamwise velocity profile at $Re_\theta = 1430$. Present DNS, Code-B (solid line, $N_x = 512$; dashed line, $N_x = 1024$); experimental data of DeGraaff and Eaton [2] (symbols).

for $\langle u_1'^2 \rangle$, 5.7% for $\langle u_3'^2 \rangle$ and 3.1% for $\langle u_1' u_3' \rangle$. However the total CPU time required for the run with the finer mesh was 9500 h, i.e. more than three times that of the original mesh, and the memory doubled to 26 Gbytes on Cray-T3E with 256 processors.
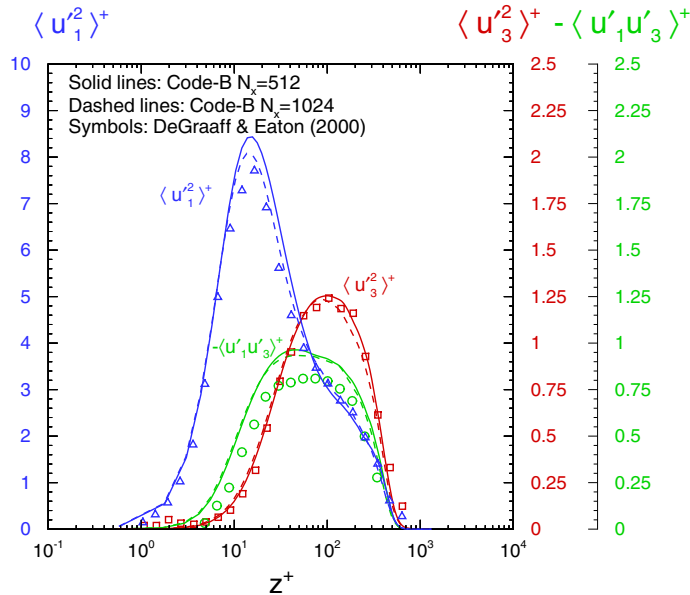
Fig. 10. Reynolds stresses profiles at $Re_\theta = 1430$. Present DNS, Code-B (solid lines, $N_x = 512$; dashed lines, $N_x = 1024$); experimental data of DeGraaff and Eaton [2] (symbols).

4. Closing remarks

We presented a method for generating inflow conditions for DNS of SDTBLs. The method is a modification of that of LWS [9]. The approach of Lund et al. is based on having an auxiliary simulation (Code-A) in a three-dimensional domain similar to that of the main simulation (Code-B). The instantaneous velocity field on a selected plane in Code-A is used as the instantaneous inflow conditions for Code-B. The inflow conditions for Code-A are generated through a sequence of operations in which the velocity field at a downstream station is rescaled and re-introduced at the inlet plane. Our modification focuses on generating the inflow conditions for Code-A and comprises two main Tasks.

Task-1 requires the prescription of the spectrum, $E(k)$, of the TKE and the vertical, z or x_3, profiles of the four velocity correlations: $\langle u_1'^2 \rangle$, $\langle u_2'^2 \rangle$, $\langle u_3'^2 \rangle$, and $\langle u_i' u_j' \rangle$. The prescribed values of $E(k)$ and $\langle u_i' u_j' \rangle$ are then used in conjunction with the method of Le and Moin [6] to obtain the velocity field $u_i(x = 0, y, z)$ at time $t = 0$. The objective of Task-1 is to create a realistic distribution of the velocity field throughout the computational domain (Code-A) which is then used as an initial condition for Task-2.

Task-2 employs LWS's rescaling method to adjust the profiles of $\langle U_i \rangle$ and $\langle u_i' u_j' \rangle$ so that they match the growth rate of the SDTBL with the prescribed value of the momentum thickness Reynolds number, Re_θ, or the boundary layer thickness Reynolds number, Re_δ, at the inlet plane.

Task-1 is the *main* difference between our method and that of LWS [9]. The combination of a realistic $E(k)$ and a non-vanishing $\langle u_1' u_3' \rangle$ in our method insures that the velocity-derivative skewness (10) maintains a value throughout the domain (Code-A) of about -0.5 as shown in Fig. 2. Our modification is essential for sustaining the production rate of TKE near the wall throughout the domain. Our DNS results obtained with the new modification are in excellent agreement with the experimental data of DeGraaff and Eaton [2] at $Re_\theta = 1430$.

Acknowledgements

Appendix A. Reference streamwise velocity profile: $U_{\mathrm{ref}}(z)$

The reference streamwise velocity, U_{ref}^+, is prescribed according to the 'law of the wall' [10]. Thus, in the *viscous sublayer*,

$$U_{\mathrm{ref}}^+ = z^+, \quad \text{for } z^+ < 5. \tag{A.1}$$

Farther from the wall, the logarithmic law of the wall [15] can be written as

$$U_{\mathrm{ref}}^+ = \frac{1}{\kappa} \ln z^+ + B + \frac{\Pi}{\kappa} W\left(\frac{z}{\delta}\right), \quad \text{for } z^+ > z_1^+ \quad \text{and} \quad z/\delta \leqslant 1, \tag{A.2}$$

where $\kappa = 0.41$ is the von Kármán constant and $B = 5.2$. The wake strength parameter, Π, whose value is flow dependent [1] is prescribed as $\Pi = 0.5$. The wake function $W(z/\delta)$ can be approximated as

$$W\left(\frac{z}{\delta}\right) = 2 \sin^2\left(\frac{\pi}{2}\frac{z}{\delta}\right). \tag{A.3}$$

In the buffer layer, the intermediate region between the viscous sublayer and the log-law region, a logarithmic law is used,

$$U_{\mathrm{ref}}^+ = 5 \ln z^+ - 3.05, \quad \text{for } z^+ > 5 \quad \text{and} \quad z^+ < z_1^+, \tag{A.4}$$

where z_1^+ represents a hypothetical coordinate which separates the buffer layer from the log-law region. We adopted $z_1^+ = 24$ since, for $Re_\delta = 8000$ used in our simulations, the specified U_{ref}^+ in the buffer layer from Eq. (A.4) and in the log-law region from Eq. (A.2) intersect at $z^+ = 24$. Outside the boundary layer the free-stream condition is used,

$$U_{\mathrm{ref}}^+ = \frac{U_\infty}{u_\tau} \quad \text{for } z/\delta > 1. \tag{A.5}$$

A cubic spline interpolation over a few z^+ has been applied between any two consecutive profiles describing U_{ref}^+ in order to avoid unphysical kinks in its derivatives $\mathrm{d}U_{\mathrm{ref}}/\mathrm{d}z$ and $\mathrm{d}^2 U_{\mathrm{ref}}/\mathrm{d}z^2$. The friction velocity u_τ can be determined by solving the *friction law* (for fixed values of Re_δ and U_∞),

$$\frac{U_\infty}{u_\tau} = \frac{1}{\kappa} \ln\left(Re_\delta \frac{u_\tau}{U_\infty}\right) + B + \frac{2\Pi}{\kappa}, \tag{A.6}$$

which is obtained from Eq. (A.2), and the condition $U_{\mathrm{ref}} = U_\infty$ at $z = \delta$. Once u_τ and U_{ref}^+ are determined, U_{ref} can be calculated and substituted in Eq. (4). In our simulations for $Re_\delta = 8000$ and $U_\infty = 1$, the solution of (A.6) gives $u_\tau = 0.0454$.

References

[1] D. Coles, The law of the wake in the turbulent boundary layer, J. Fluid Mech. 1 (1956) 191–226.
[2] D.B. DeGraaff, J.K. Eaton, Reynolds-number scaling of the flat-plate turbulent boundary layer, J. Fluid Mech. 422 (2000) 319–346.

[3] A. Ferrante, Reduction of skin friction in a microbubbles-laden spatially-developing turbulent boundary layer over a flat plate, Ph.D. Thesis, University of California, Irvine, 2004.

[4] T. Gerz, U. Shumann, S. Elghobashi, Direct numerical simulation of stratified homogeneous turbulent shear flows, J. Fluid Mech. 200 (1989) 563–594.

[5] F.H. Harlow, J.E. Welch, Numerical calculation of time-dependent viscous incompressible flow of fluid with free surface, Phys. Fluids 8 (1965) 2182–2189.

[6] H. Le, P. Moin, Direct numerical simulation of turbulent flow over a backward-facing step, Stanford University, Mechanical Engineering, Report:TF-58:17–22, December, 1994.

[7] S. Lee, S.K. Lele, P. Moin, Simulation of spatially evolving turbulence and the applicability of Taylor's hypothesis in compressible flow, Phys. Fluids A 4 (7) (1992) 1521–1530.

[8] P.S. Lowery, W.C. Reynolds, Numerical simulation of a spatially-developing, forced, plane mixing layer, Stanford University, Mechanical Engineering, Report:TF-26, September, 1986.

[9] T.S. Lund, X. Wu, K.D. Squires, Generation of turbulent inflow data for spatially-developing boundary layer simulations, J. Comput. Phys. 140 (1998) 233–258.

[10] L. Prandtl, Bericht über die Entstehung der Turbulenz, Z. Angew. Math. Mech. 5 (1925) 136–139.

[11] H. Schmidt, U. Schumann, H. Volkert, Three dimensional, direct and vectorized elliptic solvers for various boundary conditions, Technical Report 84-15, DFVLR-Mitt, 1984.

[12] U. Schumann, T. Hauf, H. Höller, H. Schmidt, H. Volkert, A mesoscale model for the simulation of turbulence, clouds and flow over mountains: formulation and validation examples, Beitr. Phys. Atmosph. 60 (4) (1987) 413–446.

[13] P.R. Spalart, Direct simulation of a turbulent boundary layer up to $R_\theta = 1410$, J. Fluid Mech. 187 (1988) 61–98.

[14] P.R. Spalart, A. Leonard, Direct numerical simulation of equilibrium turbulent boundary layers, in: Proceedings of the Fifth Symposium on Turbulent Shear Flows, Ithaca, NY, 1985.

[15] T. von Kármán, Mechanische ähnlichkeit und Turbulenz, in: Proceedings of the Third International Congress, Applied Mechanics, 1930, pp. 85–105.

[16] R.B. Wilhelmson, J.H. Ericksen, Direct solutions for Poisson's equation in three dimensions, J. Comput. Phys. 25 (1977) 319–331.